

Computational Design of [SiO–GeO] and [SiO–SnO] Nanoclusters for Alkaline Earth Metal Ion Transport

Fateme Mollaamin^{1,*} 

¹ Department of Biomedical Engineering, Faculty of Engineering and Architecture, Kastamonu University, Kastamonu, Turkey

* Correspondence: fmollaamin@kastamonu.edu.tr;

Received: 16.06.2025; Accepted: 1.11.2025; Published: 20.12.2025

Abstract: In this article, the promising alternative alkaline earth metals of beryllium-ion, magnesium-ion, and calcium-ion are discussed. This paper reports the transport pathway for Mg^{2+} – Be^{2+} and Mg^{2+} – Ca^{2+} hybrid ions. Functionalizing of Mg, Be, Ca atoms can augment the negative atomic charge of O2, O3, O7–O12, O14, O15, O17, O18, O22–O27, O29, O30 in $Mg^{2+}Be^{2+}[SiO-GeO]$, $Mg^{2+}Ca^{2+}[SiO-GeO]$, $Mg^{2+}Be^{2+}[SiO-SnO]$, $Mg^{2+}Ca^{2+}[SiO-SnO]$ nanoclusters. Improving the thermoelectric efficiency of such materials is achieved by simultaneously increasing the electrical conductance (G) within the highest occupied molecular orbital (HOMO) and lowest unoccupied molecular orbital (LUMO) gap. The electronic states of carbon sites in [SiO–SnO] near the valence band have an electron acceptor character, while metal ion sites have an electron donor character. The current study aims to delve deeper into several aspects of this molecular entity, including describing its structure and mode of operation at the atomic level, understanding its molecular and functional diversity, and examining the consequences of its malfunction due to structural alterations. Finally, the future trends of [SiO–GeO] or [SiO–SnO] in the biological field, along with the challenges encountered in realizing these technologies, are illustrated.

Keywords: bio-interface; electronic states; Mg^{2+} – Be^{2+} ; Mg^{2+} – Ca^{2+} ; ion transport; Si–Ge/Sn oxide; density of states.

© 2025 by the authors. This article is an open-access article distributed under the terms and conditions of the Creative Commons Attribution (CC BY) license (<https://creativecommons.org/licenses/by/4.0/>), which permits unrestricted use, distribution, and reproduction in any medium, provided the original work is properly cited. The authors retain copyright of their work, and no permission is required from the authors or the publisher to reuse or distribute this article, as long as proper attribution is given to the original source.

1. Introduction

While prominently represented in the environment, lithium ions are not essential cofactors in biological systems. In contrast, sodium, potassium, calcium, and magnesium are essential cofactors in multiple biological systems, while others, such as iron, zinc, and copper, play roles in specific systems [1–5]. Thus, lithium ions appear to have been isolated from being incorporated as an essential element during the evolution of increasingly complex biological systems [6–10]. The targeted delivery of therapeutics to internal organs, for example, promotes healing or apoptosis and holds promise in the treatment of numerous diseases. Currently, the prevailing delivery modality relies on circulation; however, this modality has substantial efficiency, safety, and/or controllability limitations [11–15].

Nanomaterials with distinctive structures are being investigated for their potential in electrocatalysis, fuel cells, and energy-saving applications [16–19].

Engineered noble-metal nanomaterials possess tunable optical, electrical, and biocompatible properties, making them excellent tools for probing the nanobio interface. Understanding their interactions with biomolecules, cells, and tissues at the nanobio interface is crucial for designing these nanomaterials for biomedical applications. The related action mechanisms include the kinetic and thermodynamic processes of the nano-bio-interface, the driving forces for its formation, and the chemical reactions at the nano-bio-interface. Finally, the future trends of noble metal nanomaterials in the biological field and the challenges encountered in realizing these technologies are discussed [20].

This investigation wants to delve into the feasibility of alkaline earth metal cations delivery by [SiO–GeO] or [SiO–SnO] nanocluster through formation of $Mg^{2+}Be^{2+}[SiO-GeO]$, $Mg^{2+}Be^{2+}[SiO-SnO]$, $Mg^{2+}Ca^{2+}[SiO-GeO]$, or $Mg^{2+}Ca^{2+}[SiO-SnO]$ complexes. Therefore, the physico-chemical properties of the mentioned heteroclusters. Regarding this context, [SiO–GeO] or [SiO–SnO] nanocluster was modeled with hybrid alkaline earth metal cations of $Mg^{2+}/Be^{2+}/Ca^{2+}$ as cathode materials for comparison. Following in-depth characterization, samples were measured for their performance correlated with chemical composition variations to evaluate their potency for the first time in $Mg^{2+}-Be^{2+}$ and $Mg^{2+}-Ca^{2+}$ -batteries. This work provides the first DFT-based evaluation of mixed SiO–GeO/SnO nanoclusters for the coordination of alkaline earth ions and their electronic properties. The objectives of this article are to elucidate the intriguing properties associated with the nano-bio-interface of [SiO–GeO] or [SiO–SnO], provide a brief overview of these clusters in advancing nanobiomedicine, and assess their potential as functional components in biomedical applications.

2. Materials and Methods

This study aims to transport alkali metal ions of Mg^{2+} , Be^{2+} , Ca^{2+} by [SiO–GeO] or [SiO–SnO] nanocluster towards formation of $Mg^{2+}Be^{2+}[SiO-GeO]$, $Mg^{2+}Be^{2+}[SiO-SnO]$, $Mg^{2+}Ca^{2+}[SiO-GeO]$ or $Mg^{2+}Ca^{2+}[SiO-SnO]$ complexes (Figure 1 a,b,c,d) which can increase the ion transfer in human cells. Figures 1(a,b,c,d) show alkaline earth metals-based nanoclusters of $Mg^{2+}Be^{2+}[SiO-GeO]$, $Mg^{2+}Be^{2+}[SiO-SnO]$, $Mg^{2+}Ca^{2+}[SiO-GeO]$, and $Mg^{2+}Ca^{2+}[SiO-SnO]$, which can enhance the ion delivery in body cells, transistors, or other semiconducting devices. In this research article, calculations were performed at the "CAM–B3LYP–D3" level of theory. Dispersion forces were considered under the "DFT–D3" method of Grimme with Becke–Johnson damping with multiplicity of +1 and convergence on RMS density matrix=1.00D–08 and convergence on MAX density matrix=1.00D–06 [21–24].

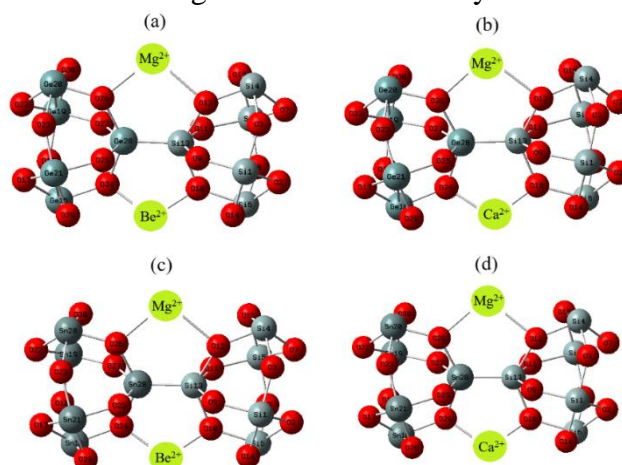


Figure 1. Delivery of Mg^{2+} , Be^{2+} , Ca^{2+} in the body cell by [SiO–(GeO/SnO)] nanoclusters and formation of (a) $Mg^{2+}Be^{2+}[SiO-GeO]$; (b) $Mg^{2+}Ca^{2+}[SiO-GeO]$; (c) $Mg^{2+}Be^{2+}[SiO-SnO]$; (d) $Mg^{2+}Ca^{2+}[SiO-SnO]$ complexes.

The analysis of Bader charge parameter [25] has been illustrated for H₂-captured hybrid clusters of Mg²⁺Be²⁺[SiO–GeO], Mg²⁺Be²⁺[SiO–SnO], Mg²⁺Ca²⁺[SiO–SnO] and Mg²⁺Ca²⁺[SiO–SnO] due to Gaussian 16 revision C.01 [26] and GaussView 6.1 program [27] (Figure1a,b,c,d).

(Ge/Sn)-containing SiO nanocluster as anodes/cathodes in magnesium batteries provides several potential Mg ion storage ways in a stable [SiO–(GeO/SnO)] anode material, increased electrical conductivity from Ge/Sn, and surface area from the nanocluster morphology.

3. Results and Discussion

3.1. Charge density differences analysis.

In Figures 2(a,b,c,d), charge density differences (CDD) [28] have been shown for Mg²⁺Be²⁺[SiO–GeO], Mg²⁺Ca²⁺[SiO–GeO], Mg²⁺Be²⁺[SiO–SnO], Mg²⁺Ca²⁺[SiO–SnO] nanoclusters with the vibration in the district about –12 to +6/+10 Bohr. Moreover, the elements of O2, O3, O7–O12, O14, O15, O17, O18, O22–O27, O29, O30 from Mg-based alloys of Mg²⁺Be²⁺[SiO–GeO], Mg²⁺Ca²⁺[SiO–GeO], Mg²⁺Be²⁺[SiO–SnO], Mg²⁺Ca²⁺[SiO–SnO] have displayed the vibration about –12 to +6/+10 Bohr (Figures 2a,b,c,d).

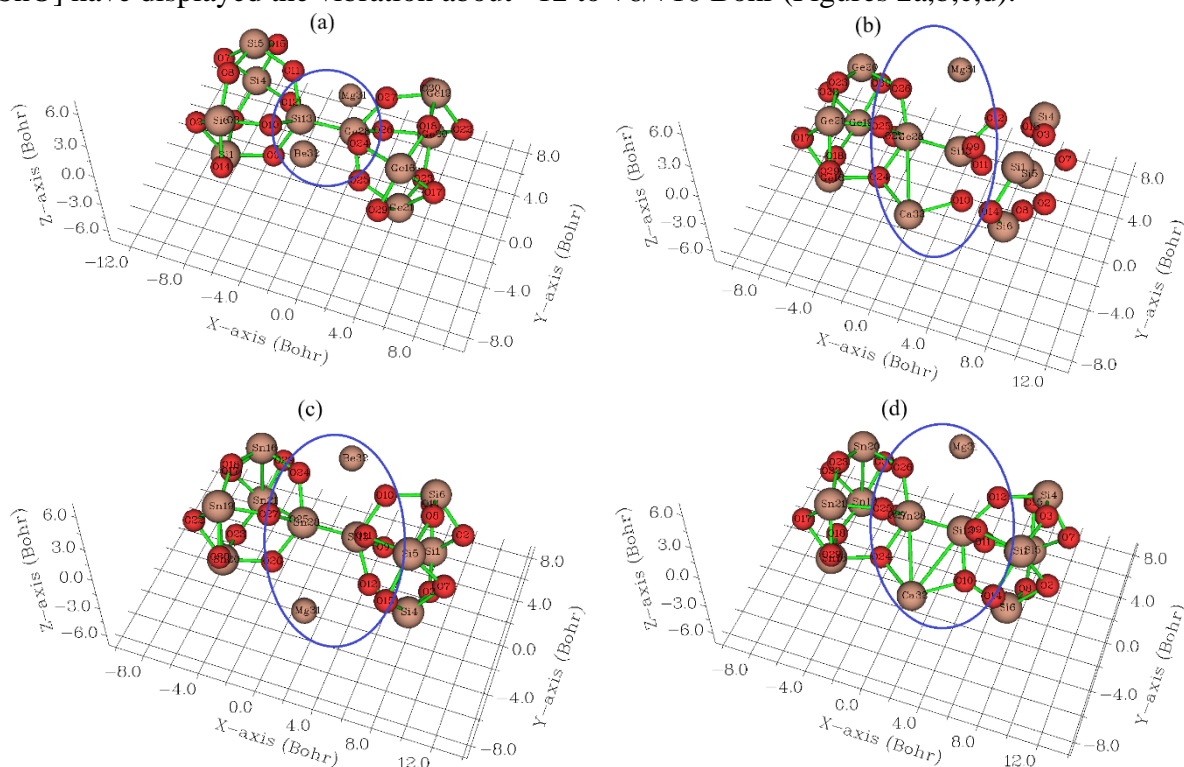


Figure 2. CDD graphs for (a) Mg²⁺Be²⁺[SiO–GeO]; (b) Mg²⁺Ca²⁺[SiO–GeO]; (c) Mg²⁺Be²⁺[SiO–SnO]; (d) Mg²⁺Ca²⁺[SiO–SnO], nanoclusters.

The charge distribution has been illustrated by Mg²⁺Be²⁺[SiO–GeO], Mg²⁺Ca²⁺[SiO–GeO], Mg²⁺Be²⁺[SiO–SnO], Mg²⁺Ca²⁺[SiO–SnO] nanoclusters (Tables 1 and 2). Functionalizing of Mg, Be, Ca atoms can augment the negative atomic charge of O2, O3, O7–O12, O14, O15, O17, O18, O22–O27, O29, O30 in Mg²⁺Be²⁺[SiO–GeO], Mg²⁺Ca²⁺[SiO–GeO], Mg²⁺Be²⁺[SiO–SnO], Mg²⁺Ca²⁺[SiO–SnO] nanoclusters.

Electronic metal–carbon interaction plays a fundamental role in tuning the electrocatalytic behavior of the metal active phase. The basis of the metal–nonmetal interaction

is the presence of topological and structural defects, as well as the heteroatom functional group silicon, which breaks the perfect symmetry of a graphene layer, providing preferential nucleation and growth sites for metal nanoparticles and a single metal site. As shown in Figure 2, the electronic states of carbon sites in [SiO–SnO] near the valence band exhibit an electron-acceptor character, whereas metal-ion sites exhibit an electron-donor character.

Table 1. The atomic charge (Q/coulomb) for Mg²⁺Be²⁺[SiO–GeO], Mg²⁺Be²⁺[SiO–GeO].H₂, Mg²⁺Ca²⁺[SiO–GeO], Mg²⁺Ca²⁺[SiO–GeO].H₂ nanoclusters.

Mg ²⁺ Be ²⁺ [SiO–GeO]		Mg ²⁺ Ca ²⁺ [SiO–GeO]	
Atom	Q	Atom	Q
O2	-0.67	O2	-0.68
O3	-0.83	O3	-0.83
O7	-0.67	O7	-0.67
O8	-0.85	O8	-0.84
O9	-0.81	O9	-0.82
O10	-0.96	O10	-1.23
O11	-0.83	O11	-0.83
O12	-1.01	O12	-1.02
O14	-0.75	O14	-0.78
O15	-0.77	O15	-0.77
O17	-0.63	O17	-0.63
O18	-0.80	O18	-0.78
O22	-0.68	O22	-0.69
O23	-0.79	O23	-0.79
O24	-0.91	O24	-1.18
O25	-0.80	O25	-0.81
O26	-0.98	O26	-0.98
O27	-0.83	O27	-0.81
O29	-0.74	O29	-0.80
O30	-0.73	O30	-0.72
Mg31	1.28	Mg31	1.25
Be32	0.98	Ca32	1.73

Table 2. The atomic charge (Q/coulomb) for Mg²⁺Be²⁺[SiO–SnO], Mg²⁺Be²⁺[SiO–SnO].H₂, Mg²⁺Ca²⁺[SiO–SnO], Mg²⁺Ca²⁺[SiO–SnO].H₂ nanoclusters.

Mg ²⁺ Be ²⁺ [SiO–SnO]		Mg ²⁺ Ca ²⁺ [SiO–SnO]	
Atom	Q	Atom	Q
O2	-0.6719	O2	-0.6895
O3	-0.8351	O3	-0.8320
O7	-0.6886	O7	-0.6830
O8	-0.8536	O8	-0.8450
O9	-0.8227	O9	-0.8304
O10	-0.9564	O10	-1.2393
O11	-0.8390	O11	-0.8324
O12	-1.0083	O12	-1.0091
O14	-0.7749	O14	-0.8001
O15	-0.7646	O15	-0.7757
O17	-0.8062	O17	-0.7944
O18	-0.8870	O18	-0.8719
O22	-0.8309	O22	-0.8107
O23	-0.8919	O23	-0.8810
O24	-0.9885	O24	-1.2527
O25	-0.9185	O25	-0.9201
O26	-1.0596	O26	-1.0678
O27	-0.9570	O27	-0.9403
O29	-0.8873	O29	-0.9249
O30	-0.8926	O30	-0.8887
Mg31	1.1567	Mg31	1.1344
Be32	0.9065	Ca32	1.7117

3.2. Total density of states.

In an isolated system, the energy levels are discrete, and the concept of "density of states (DOS)" is supposed in this situation through the "Multiwfn" program [29,30]. Furthermore, the curve map of "broadened partial DOS (PDOS)" and "overlap DOS (OPDOS)" is valuable for visualizing orbital composition analysis. The curve is the "TDOS" simulated based on the distribution of "MO" energy levels. $\text{Mg}^{2+}\text{Be}^{2+}[\text{SiO-GeO}]$, $\text{Mg}^{2+}\text{Ca}^{2+}[\text{SiO-GeO}]$, $\text{Mg}^{2+}\text{Be}^{2+}[\text{SiO-SnO}]$, $\text{Mg}^{2+}\text{Ca}^{2+}[\text{SiO-SnO}]$ (Figures 3a,b,c,d) have shown the steepest maximums TDOS surrounding -0.30 , -0.40 , and -0.60 a.u. owing to covalent bond between $\text{Mg}^{2+}/\text{Be}^{2+}$ and $\text{Mg}^{2+}/\text{Ca}^{2+}$ with $[\text{SiO}-(\text{GeO}/\text{SnO})]$ nanocluster with maximum density of state of ≈ 22 .

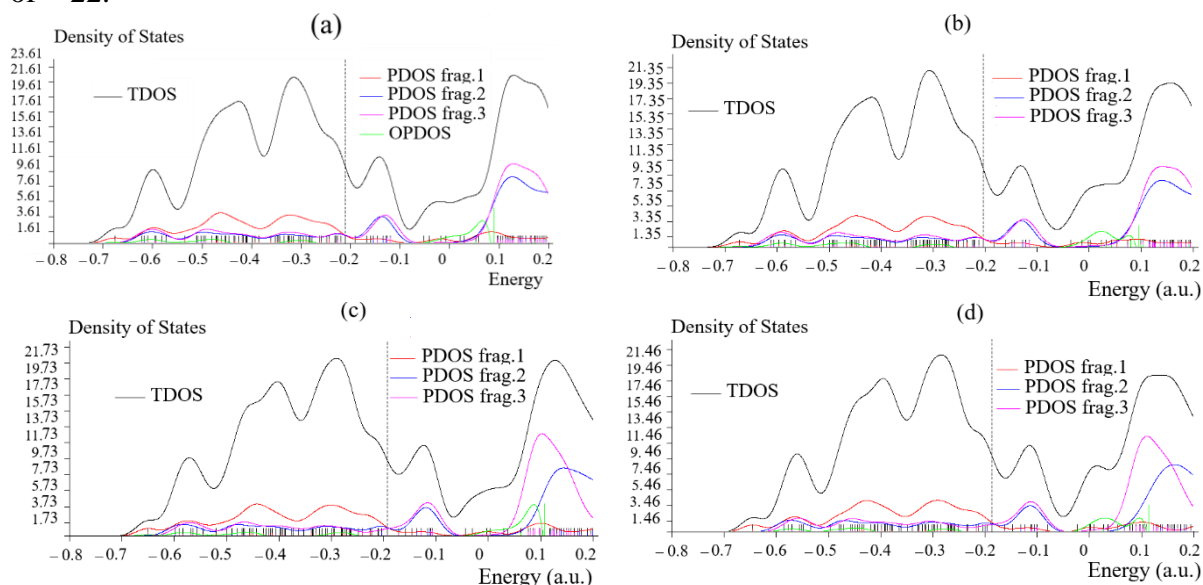


Figure 3. OPDOS/PDOS/TDOS graphs of (a) $\text{Mg}^{2+}\text{Be}^{2+}[\text{SiO-GeO}]$; (b) $\text{Mg}^{2+}\text{Ca}^{2+}[\text{SiO-GeO}]$; (c) $\text{Mg}^{2+}\text{Be}^{2+}[\text{SiO-SnO}]$; (d) $\text{Mg}^{2+}\text{Ca}^{2+}[\text{SiO-SnO}]$, nanoclusters.

Fragment 1 has been defined for O9 to O12, Si13, O24 to O27 and Ge28, $\text{Mg}^{2+31}/\text{X}32$ ($\text{Y}=\text{Be}^{2+}$, Ca^{2+}) in Figure 3 (a–d). Fragment 2 has indicated the fluctuation of Si1, Si4, and Si6 beside the similar involved atoms of Fragment 1 in Figure 3. Finally, it was considered the fluctuation of Ge16/Sn16, Ge19/Sn19 to Ge21/Sn21, O17, O18, O22, O23, O29, O30 in Figure 3 (a–d) through Fragment 3.

3.3. Localized orbital locator analysis.

Localized orbital locator (LOL) [31] has a similar expression compared to "electron localization function (ELF)" [32]. In addition, the "Multiwfn" program [29,30] supports the approximate version of "LOL" defined by "Tsilerson and Stash" [33]. Delivery of alkaline earth metal cations by $\text{Mg}^{2+}\text{Be}^{2+}[\text{SiO-GeO}]$, $\text{Mg}^{2+}\text{Ca}^{2+}[\text{SiO-GeO}]$, $\text{Mg}^{2+}\text{Be}^{2+}[\text{SiO-SnO}]$, $\text{Mg}^{2+}\text{Ca}^{2+}[\text{SiO-SnO}]$ nanoclusters (Figure 4a,b,c,d) might be described by LOL graphs using Multiwfn program [29,30] due to the delocalization/localization of electrons and chemical bonds (Figure 4a,b,c,d).

$\text{Mg}^{2+}\text{Be}^{2+}[\text{SiO-GeO}]$ (Figure 4a), $\text{Mg}^{2+}\text{Ca}^{2+}[\text{SiO-GeO}]$ (Figure 4b), $\text{Mg}^{2+}\text{Be}^{2+}[\text{SiO-SnO}]$ (Figure 4c), $\text{Mg}^{2+}\text{Ca}^{2+}[\text{SiO-SnO}]$ (Figure 4d) have demonstrated the electron delocalization through an isosurface map with labeling atoms of O10, O12, Si13, O24, O26, Ge28 or Sn28, X(31)($\text{X}=\text{Mg}^{2+}$), Y(32) ($\text{Y}=\text{Be}^{2+}$ or Ca^{2+}).

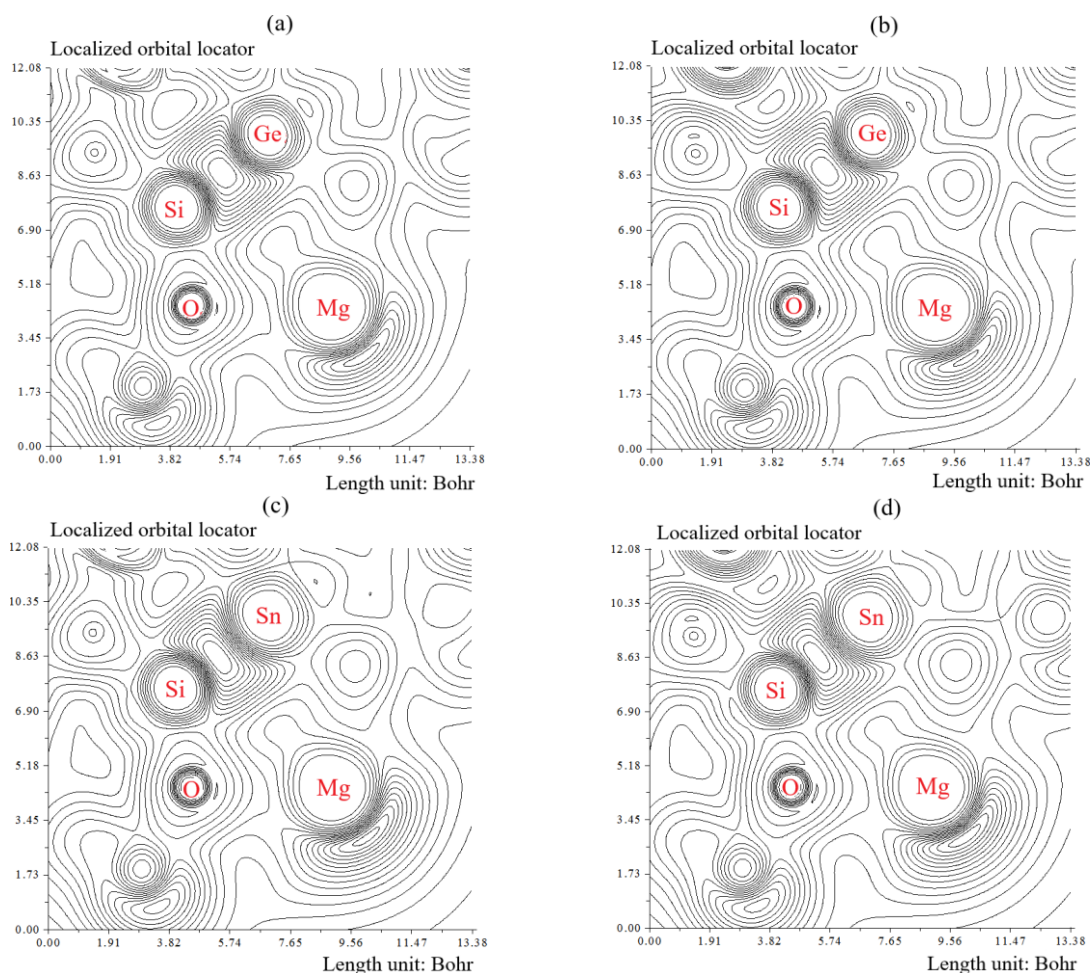


Figure 4. The shaded map of LOL graphs for (a) $\text{Mg}^{2+}\text{Be}^{2+}[\text{SiO-GeO}]$; (b) $\text{Mg}^{2+}\text{Ca}^{2+}[\text{SiO-GeO}]$; (c) $\text{Mg}^{2+}\text{Be}^{2+}[\text{SiO-SnO}]$; (d) $\text{Mg}^{2+}\text{Ca}^{2+}[\text{SiO-SnO}]$, nanoclusters.

Improving the thermoelectric efficiency of such materials is achieved by simultaneously increasing the electrical conductance (G) within the highest occupied molecular orbital (HOMO) and lowest unoccupied molecular orbital (LUMO) gap (Table 3).

Table 3. Stability energy (kcal/mol), dipole moment (debye), LUMO (eV), HOMO(eV), and energy gap (ΔE) (eV) for $\text{Mg}^{2+}\text{Be}^{2+}[\text{SiO-GeO}]$, $\text{Mg}^{2+}\text{Ca}^{2+}[\text{SiO-GeO}]$, $\text{Mg}^{2+}\text{Be}^{2+}[\text{SiO-SnO}]$, $\text{Mg}^{2+}\text{Ca}^{2+}[\text{SiO-SnO}]$ heteroclusters.

Heteroclusters	$E_s \times 10^{-3}$ (kcal/mol)	Dipole moment (debye)	E_{HOMO} (eV)	E_{LUMO} (eV)	$\Delta E = E_{\text{LUMO}} - E_{\text{HOMO}}$ (eV)
$\text{Mg}^{2+}\text{Be}^{2+}[\text{SiO-GeO}]$	-976.91	3.45	-5.74	-5.18	0.56
$\text{Mg}^{2+}\text{Ca}^{2+}[\text{SiO-GeO}]$	-990.58	0.98	-5.52	-4.94	0.58
$\text{Mg}^{2+}\text{Be}^{2+}[\text{SiO-SnO}]$	-975.28	7.44	-5.24	-4.65	0.59
$\text{Mg}^{2+}\text{Ca}^{2+}[\text{SiO-SnO}]$	-988.95	6.35	-5.08	-4.43	0.64

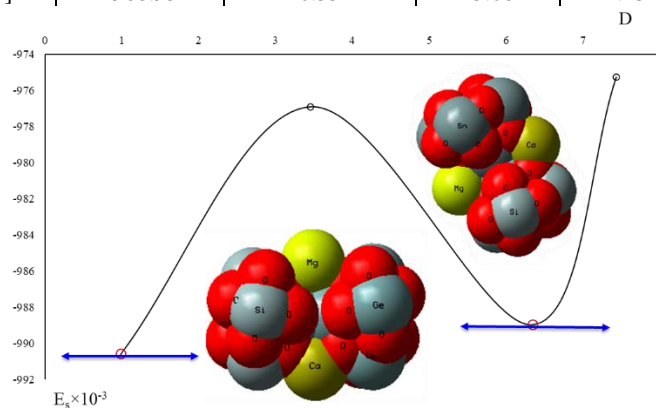


Figure 5. The changes of stability energy ($E_s \times 10^{-3} / \text{kcal.mol}^{-1}$) versus dipole moment (D/debye) for $\text{Mg}^{2+}\text{Be}^{2+}[\text{SiO-GeO}]$, $\text{Mg}^{2+}\text{Ca}^{2+}[\text{SiO-GeO}]$, $\text{Mg}^{2+}\text{Be}^{2+}[\text{SiO-SnO}]$ and $\text{Mg}^{2+}\text{Ca}^{2+}[\text{SiO-SnO}]$ nanoclusters (Table 3).

Furthermore, the stability energy versus dipole moment for interaction between Mg-, Be-, Ca- cations and [SiO–GeO] or [SiO–SnO] heterocluster has been indicated in Figure 5.

4. Conclusions

Delivery of alkaline earth metal cations of Mg²⁺, Be²⁺, or Ca²⁺ in the body cells by heterocluster of [SiO–GeO] or [SiO–SnO] towards formation of Mg²⁺Be²⁺[SiO–GeO], Mg²⁺Ca²⁺[SiO–GeO], Mg²⁺Be²⁺[SiO–SnO], Mg²⁺Ca²⁺[SiO–SnO] complexes was studied by computational method. Computational design can be used to establish a surface-state model of the interaction between [SiO–(GeO/SnO)] clusters and ion transfer in the body, ensuring safety and effectiveness. Therefore, future research should pay more attention to theoretical simulations to accurately and in-depth study nanobiointeractions, paving the way for safe and effective biomedical applications of the bio-interface of [SiO–(GeO/SnO)] clusters.

Institutional Review Board Statement

Not applicable.

Informed Consent Statement

Not applicable.

Data Availability Statement

Data supporting the findings of this study are available upon reasonable request from the corresponding author.

Funding

This research received no external funding.

Acknowledgments

In successfully completing this paper and its research, the author is grateful to Kastamonu University.

Conflict of Interest

The author declares no conflict of interest.

References

1. Hart, D.A. Lithium Ions as Modulators of Complex Biological Processes: The Conundrum of Multiple Targets, Responsiveness and Non-Responsiveness, and the Potential to Prevent or Correct Dysregulation of Systems during Aging and in Disease. *Biomolecules* **2024**, *14*, 905, <https://doi.org/10.3390/biom14080905>.
2. Herrera-Rivero, M.; Gutierrez-Fragosa, K.; International consortium on lithium genetics (ConLi + Gen); Kurtz, J.; Baune, B.T. Immunogenetics of lithium response and psychiatric phenotypes in patients with bipolar disorder. *Transl. Psychiatry* **2024**, *14*, 174, <https://doi.org/10.1038/s41398-024-02865-4>.
3. Phelps, J.; Coskey, O.P. Low and very low lithium levels: Thyroid effects are small but still require monitoring. *Bipolar Disord.* **2024**, *26*, 129–135, <https://doi.org/10.1111/bdi.13377>.

4. Gelman, K.; Melott, J.; Thakur, V.; Tarabishy, A.R.; Brandt, A.; Konrad, P.; Ranjan, M.; Memon, A.A. MR-guided focused ultrasound thalamotomy for lithium-induced tremor: A case report and literature review. *Front. Neurol.* **2024**, *14*, 1331241, <https://doi.org/10.3389/fneur.2023.1331241>.
5. Singulani, M.P.; Fernandes-Ferreira, A.F.; Figueroa, P.S.; Cuyul-Vasquez, I.; Talib, L.L.; Britto, L.R.; Forlenza, O.V. Lithium and disease modification: A systematic review and meta-analysis in Alzheimer's and Parkinson's disease. *Ageing Res. Rev.* **2024**, *95*, 102231, <https://doi.org/10.1016/j.arr.2024.102231>.
6. Mollaamin, F.; Monajjemi, M. Electric and Magnetic Evaluation of Aluminum–Magnesium Nanoalloy Decorated with Germanium Through Heterocyclic Carbenes Adsorption: A Density Functional Theory Study. *Russ. J. Phys. Chem. B* **2023**, *17*, 658–672, <https://doi.org/10.1134/S1990793123030223>.
7. Richard, S.A. Elucidating the pivotal molecular mechanisms, therapeutic and neuroprotective effects of lithium in traumatic brain injury. *Brain Behav.* **2024**, *14*, e3595, <https://doi.org/10.1002/brb3.3595>.
8. Dean, B.; Scarr, E. Common changes in rat cortical gene expression after valproate or lithium treatment particularly affect pre- and post-synaptic pathways that regulate four neurotransmitters systems. *World J. Biol. Psychiatry* **2024**, *25*, 54–64, <https://doi.org/10.1080/15622975.2023.2258972>.
9. Zafrilla-Lopez, M.; Acosta-Diez, M.; Mitjans, M.; Gimenez-Palomo, A.; Saiz, P.A.; Barrot-Feixat, C.; Jimenez, E.; Papiol, S.; Ruiz, V.; Gavin, P.; et al. Lithium response in bipolar disorder: Epigenome-wide DNA methylation signatures and epigenetic aging. *Eur. Neuropsychopharmacol.* **2024**, *85*, 23–31, <https://doi.org/10.1016/j.euroneuro.2024.03.010>.
10. Kraysberg, A.; Eli, Y.E.; Biomaterials for advanced Li and Li-ion batteries. *J Solid State Electrochem.* **2025**. <https://doi.org/10.1007/s10008-025-06268-3>.
11. Zafar, M.S.; Salimi, P.; Ricci, M.; Zia, J.; Zaccaria, R.P. Environmentally Sustainable Anode Material for Lithium-Ion Batteries Derived from Cattle Bone Waste: A Full-Cell Analysis with a LiFePO₄ Cathode. *Sustainability* **2025**, *17*, 3005, <https://doi.org/10.3390/su17073005>.
12. Barbosa Nogueira, M.J.; Chauque, S.; Sperati, V.; Savio, L.; Divitini, G.; Pasquale, L.; Marras, S.; Franchi, P.; Paciornik, S.; Proietti Zaccaria, R.; et al. Untreated Bamboo Biochar as Anode Material for Sustainable Lithium Ion Batteries. *Biomass Bioenergy* **2025**, *193*, 107511, <https://doi.org/10.1016/j.biombioe.2024.107511>.
13. Müller, M.; Obuz, H.E.; Keber, S.; Tekmanli, F.; Mettke, L.N.; Yagmurlu, B. Concepts for the Sustainable Hydrometallurgical Processing of End-of-Life Lithium Iron Phosphate (LFP) Batteries. *Sustainability* **2024**, *16*, 11267, <https://doi.org/10.3390/su162411267>.
14. Seroka, N.S.; Luo, H.; Khotseng, L. Biochar-Derived Anode Materials for Lithium-Ion Batteries: A Review. *Batteries* **2024**, *10*, 144, <https://doi.org/10.3390/batteries10050144>.
15. Wei, T.; Zhou, Y.; Sun, C.; Guo, X.; Xu, S.; Chen, D.; Tang, Y. An intermittent lithium deposition model based on CuMn-bimetallic MOF derivatives for composite lithium anode with ultrahigh areal capacity and current densities. *Nano Res.* **2024**, *17*, 2763–2769, <https://doi.org/10.1007/s12274-023-6187-8>.
16. Mollaamin, F.; Monajjemi, M. Nanomaterials for Sustainable Energy in Hydrogen-Fuel Cell: Functionalization and Characterization of Carbon Nano-Semiconductors with Silicon, Germanium, Tin or Lead through Density Functional Theory Study. *Russ. J. Phys. Chem. B* **2024**, *18*, 607–623, <https://doi.org/10.1134/S1990793124020271>.
17. Mollaamin, F.; Shahriari, S.; Monajjemi, M. Influence of Transition Metals for Emergence of Energy Storage in Fuel Cells through Hydrogen Adsorption on the MgAl Surface. *Russ. J. Phys. Chem. B* **2024**, *18*, 398–418, <https://doi.org/10.1134/S199079312402026X>.
18. Mollaamin, F. Competitive Intracellular Hydrogen-Nanocarrier Among Aluminum, Carbon, or Silicon Implantation: a Novel Technology of Eco-Friendly Energy Storage using Research Density Functional Theory. *Russ. J. Phys. Chem. B* **2024**, *18*, 805–820, <https://doi.org/10.1134/S1990793124700131>.
19. Mollaamin, F. Anchoring of 2D layered materials of Ge₅Si₅O₂₀ for (Li/Na/K)-(Rb/Cs) batteries towards Eco-friendly energy storage. *BMC Chem.* **2025**, *19*, 233, <https://doi.org/10.1186/s13065-025-01593-0>.
20. Guo, P.; Wang, Y.; Cui, H.; Yao, X.; Guan, G.; Han, M.-Y. Nano-bio-interface: Unleashing the Potential of Noble Nanometals. *Small Sci.* **2024**, *4*, 2300227, <https://doi.org/10.1002/smssc.202300227>.
21. Becke, A.D. Density-functional thermochemistry. III. The role of exact exchange. *J. Chem. Phys.* **1993**, *98*, 5648–5652, <https://doi.org/10.1063/1.464913>.
22. Lee, C.; Yang, W.; Parr, R.G. Development of the Colle-Salvetti correlation-energy formula into a functional of the electron density. *Phys. Rev. B* **1988**, *37*, 785, <https://doi.org/10.1103/PhysRevB.37.785>.

23. Benalia, A.; Boukaoud, A.; Amrani, R.; Krid, A. A B3LYP-D3 computational study of electronic, structural and torsional dynamic properties of mono-substituted naphthalenes: the effect of the nature and position of substituent. *J Mol Model* **2024**, *30*, 88, <https://doi.org/10.1007/s00894-024-05884-6>.
24. Kohn, W.; Sham, L.J. Self-Consistent Equations Including Exchange and Correlation Effects. *Phys. Rev.* **1965**, *140*, A1133, <https://doi.org/10.1103/PhysRev.140.A1133>.
25. Zhou, X.; Cheng, Y.; Xu, X.; Zhang, L.; Tian, S.; Xu, X.; Guo, B.; Tang, W.; Yan, C.; Qian, T. Bader Charge Balance Mechanism Realizes Industrial-Grade Current Hydrogen Production. *Inorg. Chem.* **2025**, *64*, 14118–14127, <https://doi.org/10.1021/acs.inorgchem.5c00590>.
26. Frisch, M.J.; Trucks, G.W.; Schlegel, H.B.; Scuseria, G.E.; Robb, M.A.; Cheeseman, J.R.; Scalmani, G.; Barone, V.; Petersson, G.A.; Nakatsuji, H.; Li, X.; Caricato, M.; Marenich, A.V.; Bloino, J.; Janesko, B.G.; Gomperts, R.; Mennucci, B.; Hratchian, H.P.; Ortiz, J. V.; Izmaylov, A. F.; Sonnenberg, J.L.; Williams-Young, D.; Ding, F.; Lipparini, F.; Egidi, F.; Goings, J.; Peng, B.; Petrone, A.; Henderson, T.; Ranasinghe, D.; Zakrzewski, V.G.; Gao, J.; Rega, N.; Zheng, G.; Liang, W.; Hada, M.; Ehara, M.; Toyota, K.; Fukuda, R.; Hasegawa, J.; Ishida, M.; Nakajima, T.; Honda, Y.; Kitao, O.; Nakai, H.; Vreven, T.; Throssell, K.; Montgomery, J.A., Jr.; Peralta, J.E.; Ogliaro, F.; Bearpark, M.J.; Heyd, J.J.; Brothers, E.N.; Kudin, K.N.; Staroverov, V.N.; Keith, T.A.; Kobayashi, R.; Normand, J.; Raghavachari, K.; Rendell, A.P.; Burant, J.C.; Iyengar, S.S.; Tomasi, J.; Cossi, M.; Millam, J.M.; Klene, M.; Adamo, C.; Cammi, R.; Ochterski, J.W.; Martin, R.L.; Morokuma, K.; Farkas, O.; Foresman, J.B.; Fox, D.J. Gaussian 16, Revision C.01, Gaussian, Inc., Wallingford CT, **2016**.
27. Dennington, R.; Keith Todd, A.; Millam John, M. GaussView, Version 6.06.16. Semichem Inc., Shawnee Mission, KS, USA, **2016**.
28. Xu, Z.; Qin, C.; Yu, Y.; Jiang, G.; Zhao, L. First-principles study of adsorption, dissociation, and diffusion of hydrogen on α -U (110) surface. *AIP Adv.* **2024**, *14*, 055114, <https://doi.org/10.1063/5.0208082>.
29. Lu, T.; Chen, F. Multiwfn: A multifunctional wavefunction analyzer. *J. Comput. Chem.* **2012**, *33*, 580–592, <https://doi.org/10.1002/jcc.22885>.
30. Lu, T. A comprehensive electron wavefunction analysis toolbox for chemists, Multiwfn. *J. Chem. Phys.* **2024**, *161*, 082503, <https://doi.org/10.1063/5.0216272>.
31. Zhang, G.; Gai, X.; Sun, L.; Ma, J. Determine the Relative Aromaticity of Bilayer Graphyne, Bilayer Graphdiyne, and Bilayer Graphtriyne. *Molecules* **2025**, *30*, 365, <https://doi.org/10.3390/molecules30020365>.
32. Rathebe, P.C.; Kholopo, M. Instruments and Measurement Techniques to Assess Extremely Low-Frequency Electromagnetic Fields. *Sensors* **2025**, *25*, 4866. <https://doi.org/10.3390/s25154866>.
33. Tsirelson, V.; Stash, A. Analyzing experimental electron density with the localized-orbital locator. *Acta Cryst.* **2002**, *B58*, 780–785, <https://doi.org/10.1107/S0108768102012338>.

Publisher’s Note & Disclaimer

The statements, opinions, and data presented in this publication are solely those of the individual author(s) and contributor(s) and do not necessarily reflect the views of the publisher and/or the editor(s). The publisher and/or the editor(s) disclaim any responsibility for the accuracy, completeness, or reliability of the content. Neither the publisher nor the editor(s) assume any legal liability for any errors, omissions, or consequences arising from the use of the information presented in this publication. Furthermore, the publisher and/or the editor(s) disclaim any liability for any injury, damage, or loss to persons or property that may result from the use of any ideas, methods, instructions, or products mentioned in the content. Readers are encouraged to independently verify any information before relying on it, and the publisher assumes no responsibility for any consequences arising from the use of materials contained in this publication.